Submitted to Structures

Optimization method for shape design of auxetic bending-active gridshells using discrete differential geometry

Yusuke Sakai*, Makoto Ohsaki[a]

* Department of Architecture and Architectural Engineering, Kyoto University

Kyoto-Daigaku Katsura, Nishikyo, Kyoto 615-8540, Japan

se.sakai@archi.kyoto-u.ac.jp

[a] Department of Architecture and Architectural Engineering, Kyoto University

Abstract

The purpose of this paper is to propose an optimization method for shape design of Auxetic Bending-Active Gridshells (ABAGs). A 2-dimensional auxetic structure has negative Poisson's ratio for in-plane deformation. Positive Gaussian curvature distributed on a curved surface of ABAG is obtained by out-of-plane deformation of the initial flat grid composed of reentrant structural units. We introduce discrete differential geometry into shape design of the surface of ABAG, which can be easily discretized into triangular meshes in accordance with the discrete member locations. The objective function of the proposed optimization problem is formulated using discrete Gaussian curvature, which is defined as the angle defect at node. In addition, discrete mean curvature vector is used for specifying the direction of convexity. We use particle swarm optimization for solving the problem. It is shown in the numerical examples, that surfaces with specified distribution of convex region on an ABAG can be obtained using the proposed method.

Keywords: Auxetic structure, Bending-active gridshell, Discrete differential geometry, Particle swarm optimization

1 Introduction

Conventional structures in nature are composed of materials with positive Poisson's ratio. When they are compressed or stretched in a uniaxial direction, they expand or shrink, respectively, in the transverse direction. By contrast, the structures with negative Poisson's ratio, which are called auxetic structures, are generated by metamaterial design techniques, which artificially design materials with desirable mechanical properties [1]. An auxetic structure expands and shrinks, respectively, when it is stretched and compressed in the transverse direction [2]. Shapes of structural units of auxetic structures are generally repetitive and reentrant. Under large-deformation, each unit with negative Poisson's ratio has an effect on the deformation of the entire structure. Therefore, a design of geometry of each pattern of an auxetic structure can realize its specific property of the deformed shape.

Liu and Hu [3] stated that the purposes of designing the mechanical properties of 2- and 3-dimensional auxetic structures are i) to generate a curved surface mainly distributed by positive Gaussian curvature when subjected to out-of-plane bending, ii) to improve the resistance against shear deformation [4], iii) to improve the indentation resistance at points where concentrated loads are applied [5,6], iv) to have a high quantity of energy absorption and damping [7]. Auxetic structures can be applied to produce devices in a wide range of scales from microscale material to sports appliance, since the desired mechanical properties by engineers can be realized by tuning shapes of the structural units without changing the types of materials [8,9]. There are many researches on the mechanical properties of auxetic structures [10]. In particular, optimization is a useful tool for design of auxetic structures, since we cannot design them intuitively to realize the desired properties. Topology optimization method for continuum models based on homogenization has been used for design of microscale auxetic structures [11-13]. However, it generally causes grey-scale problems. Kureta and Kanno [14] proposed a method to solve the topology optimization problem for design of a 2-dimensional auxetic structure by using mixed-integer linear programming. They use beam elements and obtain the optimized solutions using the ground structure method.

Most researches on auxetic structures are related to the design or investigation of mechanical properties of a 2-dimensional model, or the evaluation of loading capacity or energy absorption of a 3-dimensional model. In recent years, there have been several researches of

form-finding tool taking advantage of the mechanical properties of auxetic structures. Ou *et al.* [15] proposed a new auxetic-inspired material tool 'KinetiX', which is one of the linkage mechanisms. Konaković *et al.* [16] showed a method for designing the desired shapes of a curved surface composed of a triangular linkage, which is an auxetic structure composed of triangular plates and rotational hinges. Based on Ref. [17], Chen *et al.* [18] proposed an inverse design approach for generating a curved surface composed of bistable triangular linkages with auxetic properties. However, there are still few researches on form-finding of auxetic structures in the scale of architectural roof. Furthermore, investigation is needed for practical application of a bending-active curved surface composed of an auxetic structural units.

Auxetic structures generally consist of flexible members such as beams and plates for obtaining their specific deformation properties. Among several types of deformable structures, elastic gridshell is one of the bending-active structures, which is generated by elastically bending an initial flat grid composed of flexible beams [19-21]. In this paper, Auxetic Bending-Active Gridshell (ABAG) represents a bending-active gridshell whose initial flat grid is designed as a 2-dimensional auxetic structure.

Traditionally, to construct a dome-like shape with positive Gaussian curvature, masonry or latticed shell, which is composed of short members, or continuous shell requiring many formworks has been applied [22]. By replacing these construction methods with ABAG, construction time and cost can be reduced. In addition, ABAG can be environmentally-friendly because formworks are not needed and small number of parts are used. Furthermore, it is easy to add an energy dissipation mechanism utilizing the elastic deformation of its porous shape.

Mechanical properties of ABAGs were investigated to obtain a variety of shapes of curved surfaces through the particle-spring method and finite element method [23-25]. It is also noted that in Refs. [23-25] an initial flat grid of ABAGs can be generated by additive manufacturing technique, i.e. 3D printing. Therefore, the connections between members are designed as rigid joints, which can reduce the number of structural components and the noise during deformation as compliant mechanism [26]. Designing honeycomb patterns of an initial flat grid of ABAGs by gradually increasing their values of Poisson's ratio from negative to positive is useful to obtain the desired distribution of Gaussian curvature on an ABAG [27]. By using Schwarz-Christoffel mapping, a shape of the boundary of an initial flat grid is converted from a rectangle canonical domain to physical one for generating a curved surface, which is close to the

upper-half torus. In addition, they also generate a curved surface similar to Downland gridshell [28] by ABAG composed of non-uniform honeycombs whose Poisson's ratios are tuned. Sakai and Ohsaki [29] carried out parametric study for designing ABAG with an initial flat grid with non-periodic and/or hybrid of two different reentrant patterns. Although the proposed method by Ref. [29] is a simple technique, it is useful to obtain a more complex free-form surface of an ABAG than the one composed of a uniform auxetic pattern.

A specific property of ABAG is to generate a distribution of positive Gaussian curvature, which is a geometrical invariant that can be used for designing a surface. When the absolute values of Gaussian curvature on a curved surface are too large, we obtain an unfavorable surface in view of structural or aesthetic properties. Fujita and Ohsaki [30] proposed an optimization method for designing spatial structures using geometrical invariants of a surface, which is modeled parametrically as a Bézier surface. However, it is difficult to obtain the shapes desired by designers, since a parametric surface can generate a limited class of surface shapes. Furthermore, computation of the higher-order differential coefficients with respect to the parameter is very complicated.

Higher-order differentiation of geometrical properties can be avoided using the techniques of discrete differential geometry. There are several methods for computation of discrete Gaussian curvature [31,32], among which the simplest one is the angle defect at node on a polyhedral surface [33]. Discrete Gaussian curvature measures the quantity of the convexity and concavity on a polyhedral surface. Similarly, discrete mean curvature vector [34] at node on a polyhedral surface is defined as the normal vector to the surface, whose norm is the discrete mean curvature. Therefore, discrete mean curvature vector is effective for identifying a direction of convexity at each node on a surface.

Purpose of this paper is to propose an optimization method for design of the distribution of discrete Gaussian curvature computed at each node on curved surface of an ABAG. An optimization problem for designing a curved surface obtained by large-deformation analysis can usually be formulated with highly complex functions due to geometrical nonlinearity of ABAGs. Metaheuristic algorithms can be useful tools for solving nonlinear optimization problems [35-37]. Furthermore, a sufficient number of software libraries are available for basic algorithms including Genetic Algorithm (GA) [38], Particle Swarm Optimization (PSO) [39], Simulated Annealing (SA) [40], and so on.

The remainder of this paper is organized as follows. The design method of an initial flat grid of ABAGs is proposed in Section 2. In addition, we show the effect of Poisson's ratio on the in-plane deformation of an initial flat grid and the shapes of curved surfaces generated by large-deformation analysis. In Section 3, we introduce the method of discretization of ABAGs and formulate discrete Gaussian curvature and discrete mean curvature vector [29]. In Section 4, an optimization problem is formulated for designing specified distribution of convex region on an ABAG. Finally, several numerical examples are carried out in Section 5.

2 Auxetic Bending-Active Gridshells

2.1 Design of an initial flat grid of ABAG

Structures with negative Poisson's ratio for in-plane deformation are generated by arranging periodic reentrant units which fill a plane [41]. Reentrant honeycomb [42] and reentrant triangle [11] are the two well-known units of auxetic structures [10]. As shown in Fig. 1, these reentrant units are composed of two types of members: the chevron rod consisting of multiple linear elements connected in x-direction (piecewise linear blue line) and the tie rod in y-direction (red line). The members of reentrant units are often modeled using shell elements for large-deformation analysis [23-25,27]. However, we use beam elements for modeling the members in this paper, because the use of the beam elements can reduce the computational cost for carrying out geometrically nonlinear analysis many times for optimization. It is confirmed in Sec. 2.2 that the mechanical properties of the surfaces of ABAGs can be evaluated accurately by using the beam elements.

Consider an ABAG with m chevron rods. Let θ_i $(i = 1, \ldots, m), w$, and d represent the angle between x-axis and the left-end element of the ith chevron rod, and the sizes of each reentrant unit in x- and y-directions, respectively, as shown in Fig. 1. Elastic deformation of each tie rod is smaller than that of a chevron rod during the deformation process. Bending and twisting of chevron rods have an effect on the deformed shape of an ABAG. The positive directions of θ_i of reentrant honeycombs are anti-clockwise and clockwise for odd and even i, respectively. For reentrant triangles, the positive direction of θ_i is anti-clockwise for all chevron rods. The following geometrical constraints are given for the two reentrant units:

Reentrant honeycombs: $d - \frac{1}{2}w\left(\tan\theta_i + \tan\theta_{i+1}\right) > 0,$

Reentrant triangles: $d - \frac{1}{2}w\left|\tan\theta_i - \tan\theta_{i+1}\right| > 0.$

If the left-hand side of each of the above constraint is not positive, the ith and $(i+1)$th chevron rods have contact or intersection with each other.

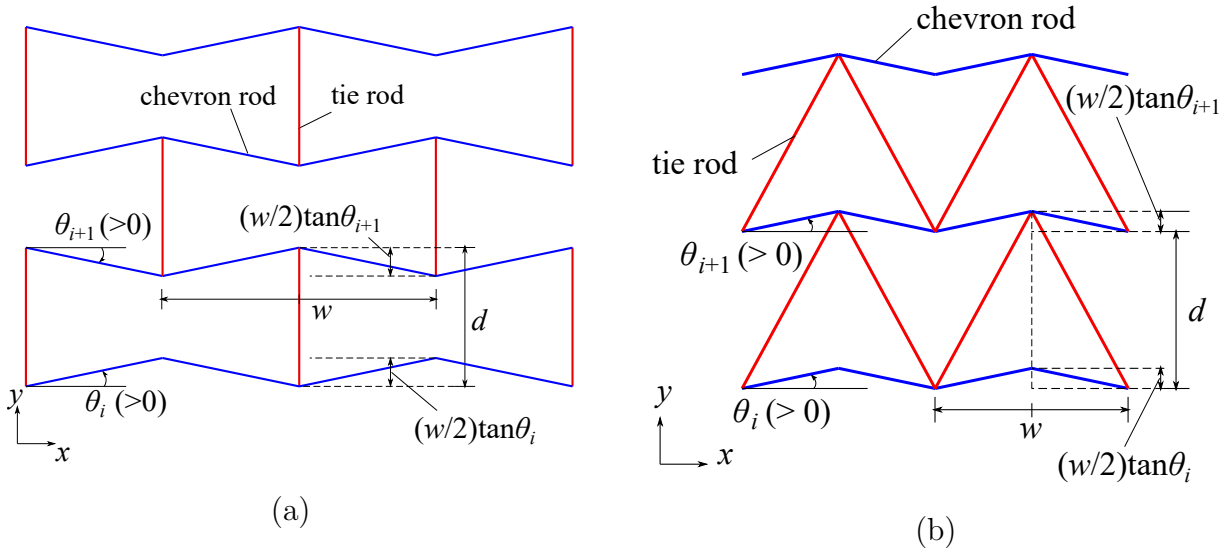

Figure 1: Reentrant units composed of the chevron rods (blue line) and the tie rods (red line) for realizing auxetic behaviors; (a) reentrant honeycomb, (b) reentrant triangle.

2.2 Poisson's ratio for in-plane deformation and Gaussian curvature on a curved surface

It is well-known that the sign of Gaussian curvature on a curved surface generated from an initial flat grid by out-of-plane deformation is dependent on the sign of Poisson's ratio for in-plane deformation of the reentrant unit [23-25,27,43,44]. Evans [44] formulated the relationship between Poisson's ratio and Gaussian curvature on a 2-dimensional auxetic structure based on plate theories. In this section, we verify the relationship by carrying out large-deformation analysis.

Figures 2(a), (b), and (c) show the in-plane (upper three figures) and out-of-plane (lower three figures) deformations from three different initial flat grids with uniform hexagonal units, which have positive, almost 0, and negative values of Poisson's ratio, respectively. The size of

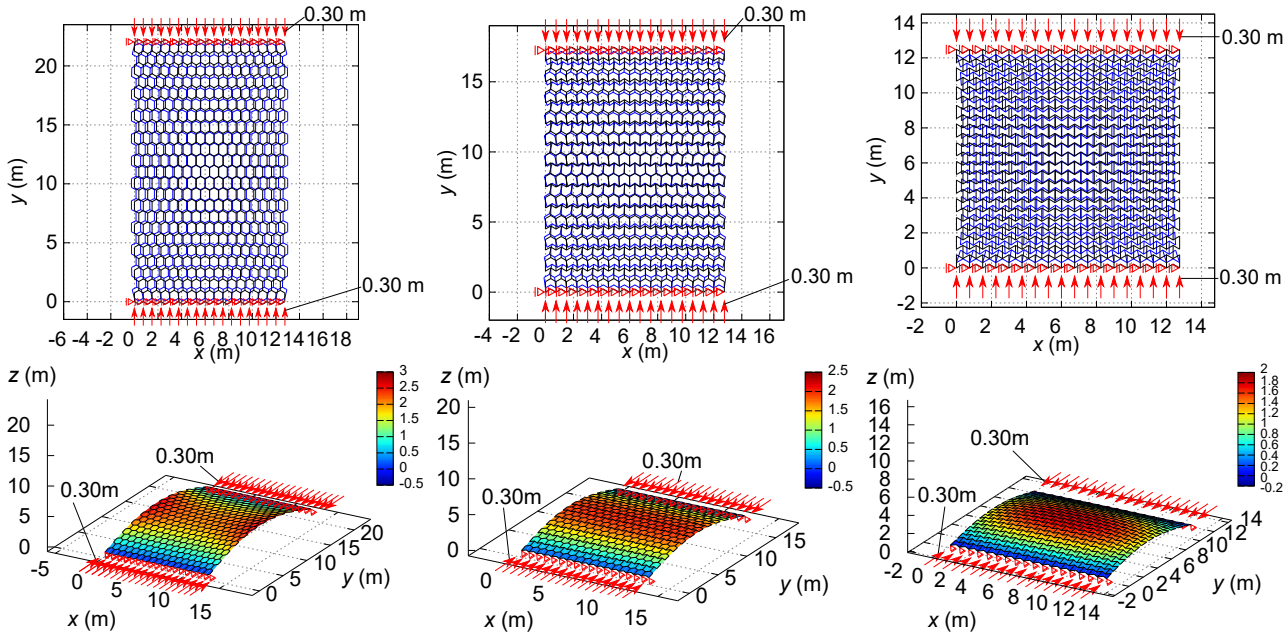

(a) (b) (c)

Figure 2: Comparison of relationships between Poisson's ratio ν and Gaussian curvature. Plan view of deformed shapes (blue) and the initial flat grid (black) for 2-dimensional case in the upper figure. Deformed shapes from an initial flat grid for 3-dimensional case in the lower figure with contour of z-directional displacement. (a) $\nu > 0$, (b) $\nu \simeq 0$, (c) $\nu < 0$.

each unit is $w = d = 0.75$ m. The width and height of cross-section of all members are 0.01 m and 0.10 m, respectively. We set $\theta_i = -\pi/6$ and $\theta_i = \pi/6$ for $\nu > 0$ and $\nu < 0$, respectively. For $\nu \simeq 0$, if i is an odd number, then $\theta_i = \pi/6$ is assigned; otherwise, $\theta_i = -\pi/6$. The connections between the tie rods and the 1st and mth chevron rods are supported with roller that can move in y-direction, as illustrated in Fig. 2. Forced displacements of 0.30 m are given at all supports in y-direction. The arrows indicate the directions of the forced displacements. For the 2-dimensional deformation, blue and black lines represent the deformed shape and the initial flat grid, respectively. To generate a curved surface, we apply the virtual upward load equal to the self-weight to all members before assigning forced displacements so that an unfavorable buckling is avoided. The vertical load is removed after the forced horizontal displacement is completed. Details of the process of large-deformation analysis is explained in Sec. 5.

Figure 2(a) shows the results of a regular honeycomb with positive Poisson's ratio. In-

plane deformation shows that the flat grid under uniaxial compression leads to expansion in the transverse direction. A shape of a curved surface composed of regular units is a saddle shape, which has negative Gaussian curvature. Figure 2(b) shows the results of an initial flat grid composed of the honeycomb unit whose Poisson's ratio is almost 0. It slightly deforms in x-direction under compression in y-direction for in-plane deformation. The obtained surface when subjected to 3-dimensional deformation is close to a developable surface, which has almost 0 Gaussian curvature. Figure 2(c) is an example of ABAG whose initial flat grid is composed of reentrant honeycombs. It shrinks in x-direction under in-plane compression in y-direction. ABAG generates a dome-like shape with positive Gaussian curvature when subjected to out-of-plane deformation.

3 Discrete Gaussian curvature and discrete mean curvature vector

Since the ABAG is modelled as a discrete frame structure, it is effective to evaluate the amount of convexity and concavity of the curved surface of ABAG as the discrete quantity without resort to a continuous parametric model of the surface. In this section, we introduce the discrete Gaussian curvature and the discrete mean curvature vector based on the discrete differential geometry [31,33], and incorporate the discrete curvatures into the optimization problem for design of ABAG.

3.1 Discretization of a curved surface of ABAG

Discrete curvature is defined for computing the curvature at node on a polyhedral surface [31,33]. Triangles based on nodal positions of discrete members of ABAG are needed for computing the discrete curvatures. In this paper, we simplify the method proposed by Ref. [29] for creating triangles on a reentrant pattern. Figure 3 shows quadrangular cones on each node composed of four triangles. Circle marks represent the nodes on the connections. The grey areas represent quadrangular cones, which are generated for all nodes except those on the boundaries.

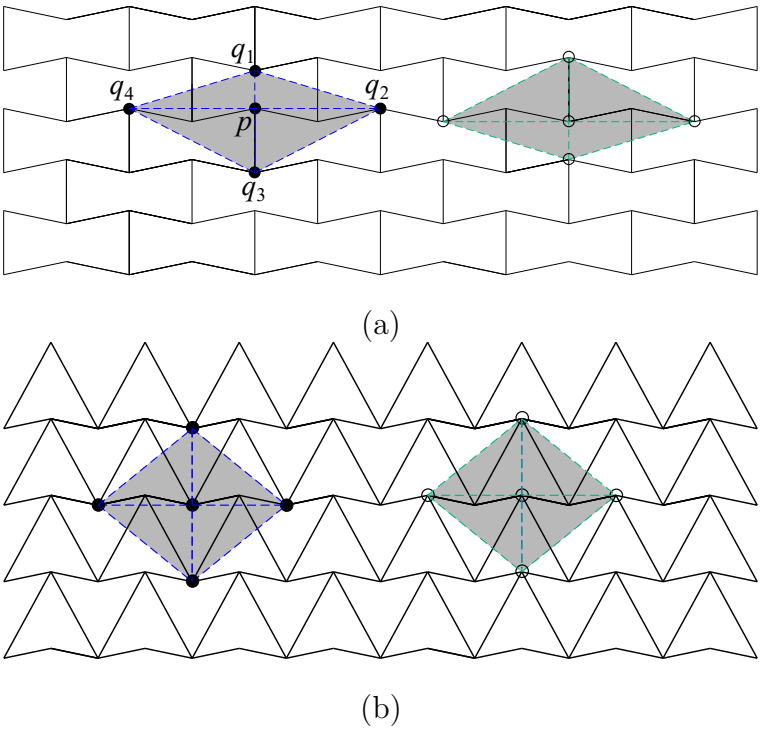

Figure 3: Quadrangular meshes composed of four triangles at each node on a curved surface of ABAG; (a) reentrant honeycomb, (b) reentrant triangle.

3.2 Discrete Gaussian curvature

Discrete Gaussian curvature is defined for computing the amount of convexity and concavity on a polyhedral surface. The correspondence between the Gaussian curvature on a continuous surface and the discrete Gaussian curvature is guaranteed by Gauss-Bonnet theory [33] related to the total curvature and topology of a surface. Figure 4 shows the quadrangular cone composed of the nodes p and q_v ($v = 1, \ldots, 4$). Let $\boldsymbol{e}_v$ denote the vector which directs from p to q_v. The grey area in Fig. 4 represents a Voronoi region produced by connecting the center of circumcircles of four surrounding triangles. Sum of the outer angles on four vertices of a Voronoi region is equal to the sum of the internal angles of four triangles at node p. Therefore, discrete Gaussian curvature is formulated as angle defect from a flat shape as follows [31,33]:

$$\begin{aligned} K_p &= 2\pi - \sum_{v=1}^{4} \phi_v \\ &= 2\pi - \sum_{v=1}^{4} \cos^{-1}\left(\frac{\boldsymbol{e}_v \cdot \boldsymbol{e}_{v+1}}{|\boldsymbol{e}_v| \cdot |\boldsymbol{e}_{v+1}|}\right). \end{aligned} \tag{1}$$

The sign of discrete Gaussian curvature at p of a quadrangular cone classifies the geomet-

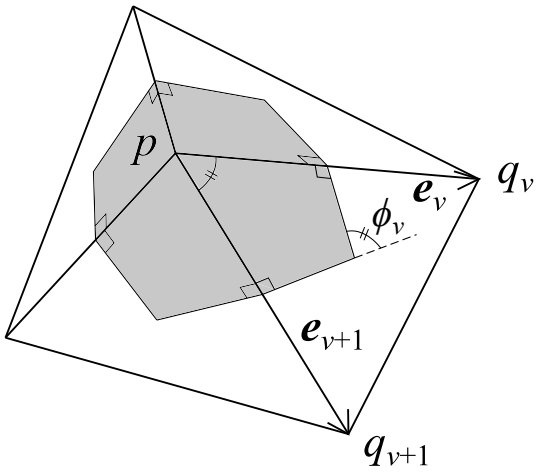

Figure 4: Quadrangular cone at node p, which is composed of four triangles corresponding to nodes q_v ($v = 1, \ldots, 4$), and Voronoi region (grey) for computing angle defect.

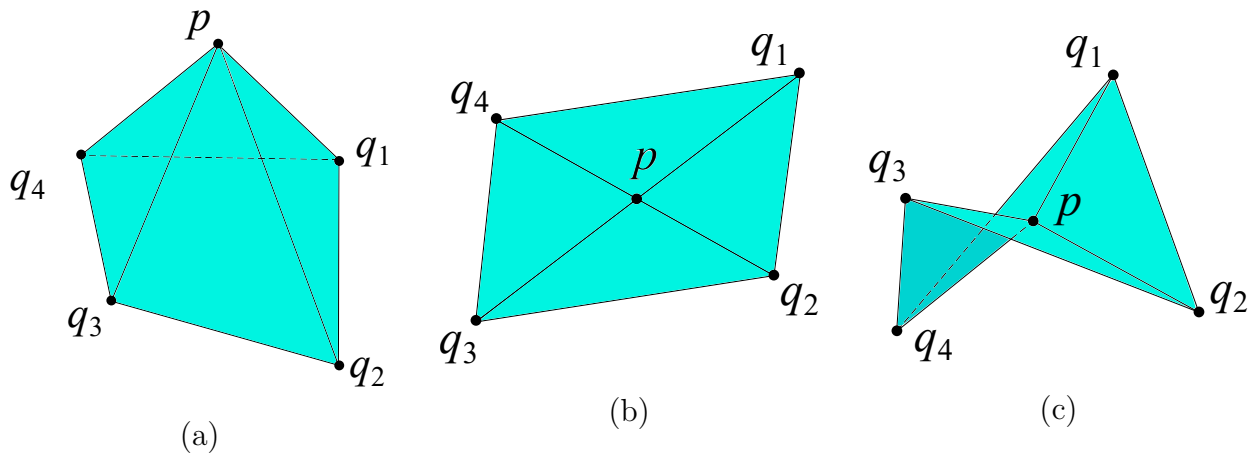

Figure 5: Shapes of quadrangular cones classified by sign of discrete Gaussian curvature; (a) $K_p > 0$, (b) $K_p = 0$, (c) $K_p < 0$.

rical relationship between p and q_v, as illustrated in Fig. 5. We obtain a cone and a saddle, respectively, for $K_p > 0$ and $K_p < 0$. A flat plane, a cylinder, or a cone is generated if $K_p = 0$.

3.3 Discrete mean curvature vector

Discrete mean curvature vector is defined as the vector in the opposite direction to the gradient of an area of four triangles. The discrete mean curvature vector $\boldsymbol{H}_p$ at node p is computed by

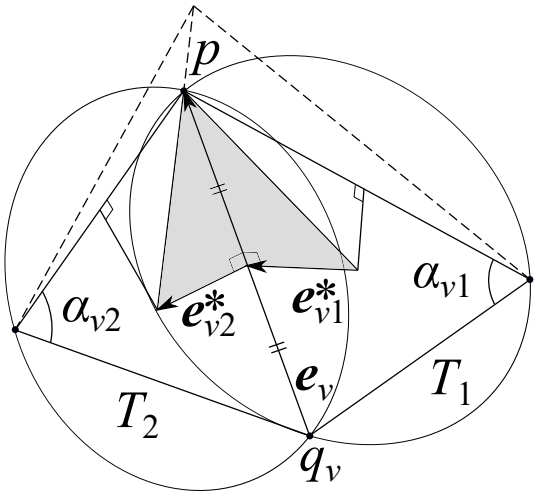

Figure 6: Vectors and angles used for cotangent formula.

the following equation proposed by Sullivan [33]:

$$\boldsymbol{H}_p = \frac{1}{2} \sum_{v=1}^{4} \left(\cot \alpha_{v1} + \cot \alpha_{v2} \right) \left(\boldsymbol{p} - \boldsymbol{q}_v \right) \tag{2}$$

Equation (2) is called cotangent formula, which is well-known in the field of discrete differential geometry [31,34]. Weight factor $(\cot \alpha_{v1} + \cot \alpha_{v2})/2$ is derived from the following geometrical relationship [32]:

$$\frac{|\boldsymbol{e}^*_{v1}| + |\boldsymbol{e}^*_{v2}|}{|\boldsymbol{e}_v|} = \frac{1}{2} \left(\cot \alpha_{v1} + \cot \alpha_{v2} \right). \tag{3}$$

Vectors $\boldsymbol{e}^*_{v1}$ and $\boldsymbol{e}^*_{v2}$ perpendicular to vector $\boldsymbol{e}_v$ connect the midpoints of the edge connecting nodes p and q_v and the centers of circumcircles of triangles T_1 and T_2, respectively, as shown in Fig. 6. Figures 7 (a), (b), and (c) show the directions of discrete mean curvature vectors $\boldsymbol{H}_p = (H^x_p, H^y_p, H^z_p)^{\mathrm{T}}$ at node p. We obtain an upward direction and a downward direction of convexity at node p, respectively, for $H^z_p > 0$ and $H^z_p < 0$, when $K_p > 0$. The vector $\boldsymbol{H}_p$ vanishes if the mean curvature is equal to 0.

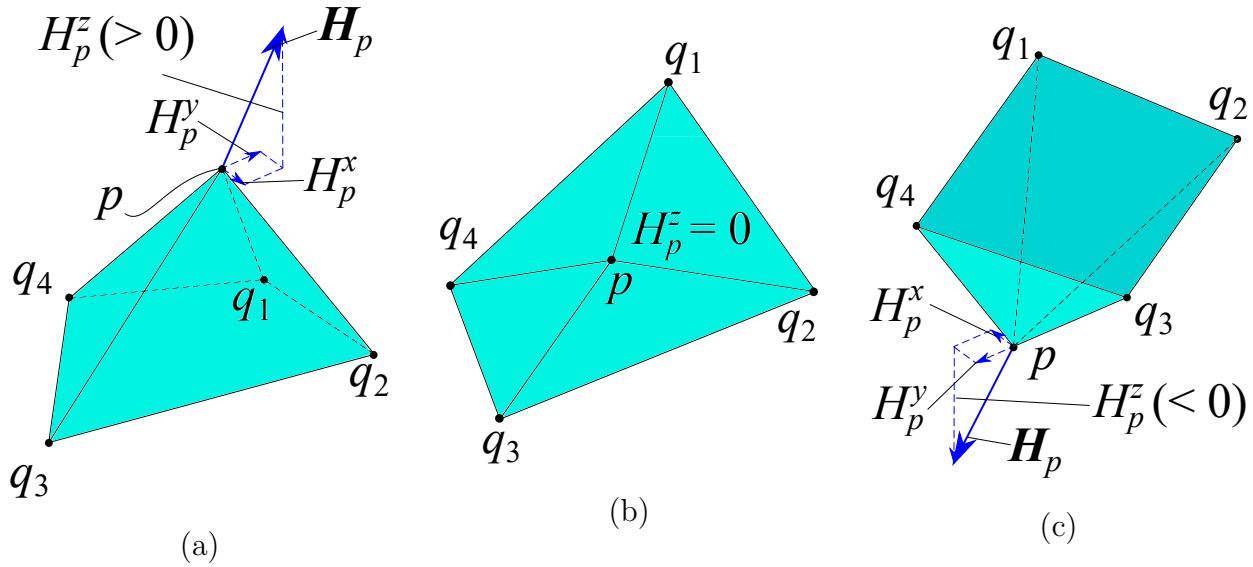

Figure 7: Directions of discrete mean curvature vectors; (a) upward direction, (b) zero mean curvature, (c) downward direction.

4 Optimization for design of distribution of discrete Gaussian curvature of ABAG

4.1 Cross-sectional heights of chevron rods

Saxena *et al.* [10] demonstrated that the value of Poisson's ratio for in-plane deformation of reentrant honeycomb is determined by the cross-sectional height and width of each member. On the other hand, according to Naboni *et al.* [23-25], distribution of the discrete Gaussian curvature on ABAG depends on the cross-sectional height of each member, as mentioned in Sec. 2.1. Therefore, the cross-sectional heights of reentrant units are tuned to obtain variable distributions of discrete Gaussian curvature of a curved surface of ABAG. Here, we set the cross-sectional height of tie rod as a constant value and those of chevron rods as variables, which are formulated by cubic Bernstein polynomials. Therefore, all cross-sectional heights of chevron rods are smoothly changed and can reduce the number of design variables by using Bernstein coefficients as design variables.

By using Bernstein coefficients β_l $(l = 0, \ldots, 3)$ and parameter u $(0 \leq u \leq 1)$, a cubic Bernstein polynomial is formulated as

$$B(u) = \beta_0 (1-u)^3 + 3\beta_1 (1-u)^2 u + 3\beta_2 (1-u) u^2 + \beta_3 u^3. \tag{4}$$

When an ABAG is composed of m chevron rods, t_{ik} represents the cross-sectional height of element k of the ith chevron rod ($i = 1, \ldots, m; k = 1, \ldots, n_i$), where n_i is the number of elements of the ith chevron rod. Let β_{li} ($l = 0, \ldots, 3$) denote the Bernstein coefficients corresponding to the ith chevron rod. Parameter u is discretized to $u_k = (k-1)/(n_i - 1)$ in terms of the element number k. We consider a symmetric structure and assume n_i is an even number. The Bernstein coefficients also satisfy $\beta_{3i} = \beta_{0i}$ and $\beta_{2i} = \beta_{1i}$ so that the distribution of cross-sectional height is symmetric. Therefore, the cross-sectional height t_{ik} is written as

$$t_{ik} = \beta_{0i}\left[(1-u_k)^3 + {u_k}^3\right] + 3\beta_{1i}\left[(1-u_k)^2 u_k + (1-u_k){u_k}^2\right], \quad u_k = \frac{k-1}{n_i - 1}. \tag{5}$$

4.2 Optimization for distribution of ratio of discrete Gaussian curvature

The purpose of this study is to present a method for obtaining the shape of ABAG that has the specific regions where the values of discrete Gaussian curvature at target nodes are increased. In this section, we formulate the optimization problem for maximizing the objective function F, which is the minimum value of discrete Gaussian curvatures K_j at each target node j ($j = 1, \ldots, N$). By solving the problem, we can obtain the optimized surface of ABAG, which has a distribution of partly maximized discrete Gaussian curvature. A condition for non-negative value of the z-component of discrete mean curvature vector $\boldsymbol{H}_j = (H_j^x, H_j^y, H_j^z)^{\mathrm{T}}$ is given at the target node j. This constraint enables us to obtain the curved surface that is upward convex at all target nodes.

The design variables are $\boldsymbol{\theta} = \{\theta_1, \ldots, \theta_m\}$, $\boldsymbol{\beta}_0 = \{\beta_{01}, \ldots, \beta_{0m}\}$, and $\boldsymbol{\beta}_1 = \{\beta_{11}, \ldots, \beta_{1m}\}$. Note that it is difficult to formulate the relationship between K_j and the design variables in an explicit form. By carrying out large-deformation analysis, we compare distributions of discrete Gaussian curvature on curved surfaces obtained with different values of three design variables θ_i, β_{0i}, and β_{1i}. Boundary conditions and forced displacements are set as explained in Sec. 5. Table 1 shows the values of θ_i, β_{0i}, and β_{1i} for Cases 1–4. Cases 1 and 2 have different arrangements of θ_i and the same values of β_{0i} and β_{1i}. On the other hand, Cases 3 and 4 have the same values of θ_i and different β_{0i} and β_{1i}. Figure 8 shows distributions of discrete Gaussian curvature and deformed surfaces of Cases 1–4 composed of reentrant honeycomb. It is clearly observed from the figure that the values of θ_i, β_{0i}, and β_{1i} have an effect on a shape

Table 1: Values of variables θ_i, β_{0i}, and β_{1i} for Cases 1–4.

Parameters	Case 1	Case 2	Case 3	Case 4
θ_8 and θ_9	0	$2\pi/9$	$\pi/6$	$\pi/6$
$\theta_i (i \neq 8 \text{ or } 9)$	$2\pi/9$	0	$\pi/6$	$\pi/6$
β_{0i} $(i = 1, \ldots, 16)$	0.10	0.10	0.01	0.30
β_{1i} $(i = 1, \ldots, 16)$	0.10	0.10	0.30	0.01

of the curved surface.

The optimization problem is formulated as follows:

$$\text{max.} \qquad F = \min_{1 \leq j \leq N} K_j \left(\boldsymbol{\theta}, \boldsymbol{\beta}_0, \boldsymbol{\beta}_1 \right) \tag{6a}$$

$$\text{subject to} \qquad H_j^z \left(\boldsymbol{\theta}, \boldsymbol{\beta}_0, \boldsymbol{\beta}_1 \right) \geq 0, \quad (j = 1, \ldots, N) \tag{6b}$$

$$\boldsymbol{\theta}^{\mathrm{L}} \leq \boldsymbol{\theta} \leq \boldsymbol{\theta}^{\mathrm{U}}, \qquad \boldsymbol{\beta}_0^{\mathrm{L}} \leq \boldsymbol{\beta}_0 \leq \boldsymbol{\beta}_0^{\mathrm{U}}, \qquad \boldsymbol{\beta}_1^{\mathrm{L}} \leq \boldsymbol{\beta}_1 \leq \boldsymbol{\beta}_1^{\mathrm{U}} \tag{6c}$$

where the upper scripts U and L indicate the upper and lower bounds of the variables, respectively. The objective function F is a highly nonlinear function of design variables. Therefore, we use PSO, which is a metaheuristic method, for solving the optimization problem without carrying out the sensitivity analysis [39]. The concept of PSO is that a large number of particles, i.e., initial solutions are generated randomly and they find the best location in the feasible region based on their local and global information.

5 Numerical examples

We carry out six numerical examples for designing a curved surface of ABAG for specified distribution of convex region. The models of Types RH and RT are composed of reentrant honeycombs and reentrant triangles, respectively.

Cross-sections of chevron rods have rectangular shapes. The cross-sectional height and width of tie rods are 0.10 m and 0.01 m, respectively. On the other hand, the cross-sectional heights are designed by Eq. (5), while their widths are fixed at 0.01 m. The lower bounds of parameters for cross-sectional heights of chevron rods are set as $\beta_0^{\mathrm{L}} = \beta_1^{\mathrm{L}} = 0.01$ m, which means that the lower bounds on cross-sectional height of chevron rod are 0.01 m. The upper

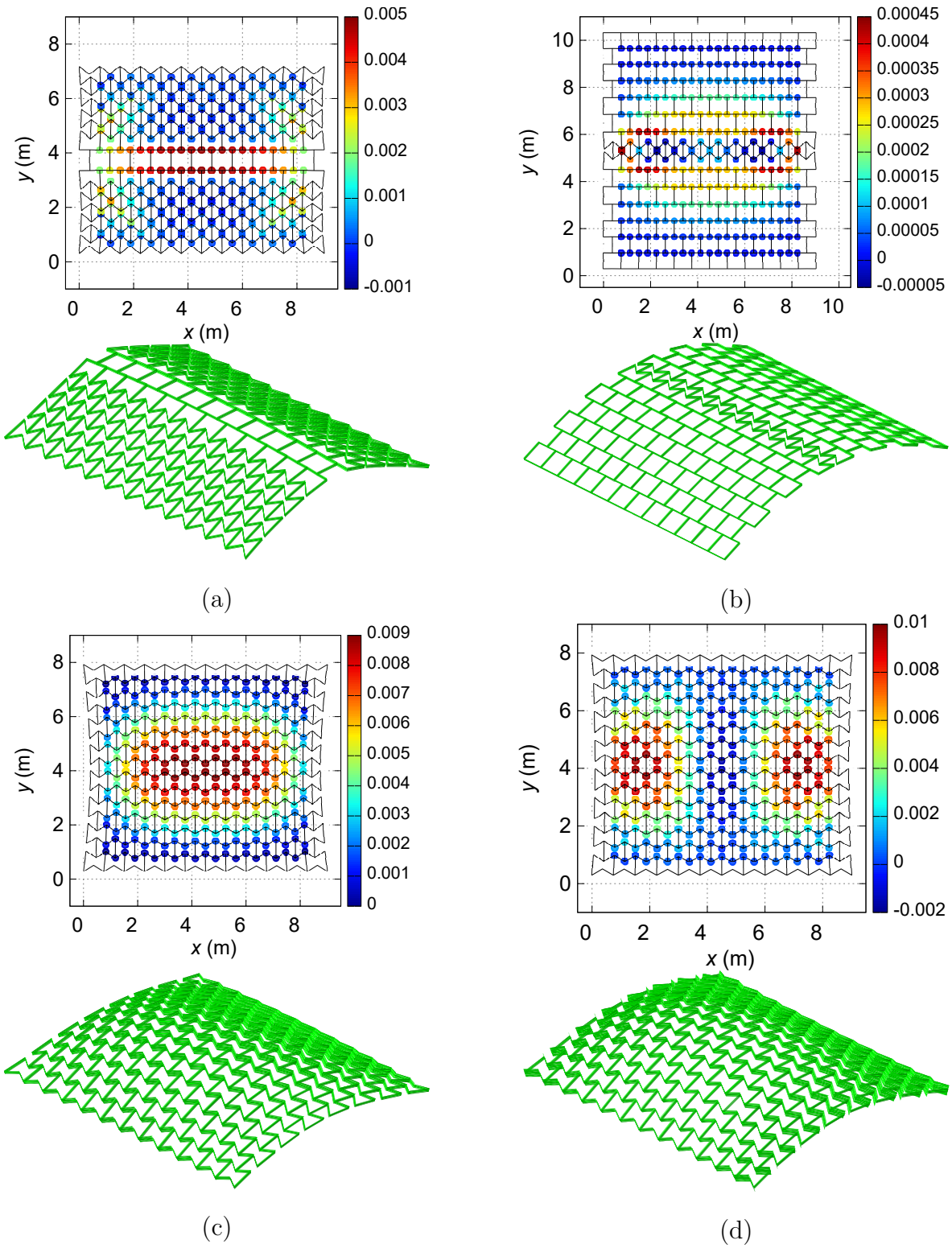

Figure 8: Distributions of discrete Gaussian curvature and shapes of curved surfaces with different values of θ_i, β_{0i}, and β_{1i}; (a) Case 1, (b) Case 2, (c) Case 3, (d) Case 4.

Table 2: Parameters for optimization of geometry and cross-section of ABAG surface.

Type	w (m)	d (m)	θ^{L}	θ^{U}	β_0^{L}	β_0^{U}	β_1^{L}	β_1^{U}
RH	0.75	0.75	0	$2\pi/9$	0.01	0.30	0.01	0.30
RT	0.60	$0.30\sqrt{3}$	0	$5\pi/18$	0.01	0.30	0.01	0.30

bounds are $\beta_0^{\mathrm{U}} = \beta_1^{\mathrm{U}} = 0.30$. Table 2 shows parameters for optimization of geometry and cross-section of ABAG surface. Here, design variables $\boldsymbol{\theta}$ are chosen as positive so that the structure has a negative Poisson's ratio. The upper bound of $\boldsymbol{\theta}$ is assigned by the geometrical constraint explained in Sec. 2.1. The details of the algorithm of PSO are explained in Appendix. The parameters of PSO are set as $\omega = 0.75$, $c_1 = 0.75$, and $c_2 = 0.5$. The number of particles and the maximum number of iterations are 100 and 30, respectively. Effect of parameter values on the optimal objective function value is investigated in Appendix.

For large-deformation analysis, we carry out a quasistatic incremental path-following analysis. The loading parameter τ is linearly increased with the maximum time increment 5.0×10^{-2} and is divided into two phases. In the period $0.0 \leq \tau \leq 1.0$, we apply the upward artificial load equal to self-weight to all members to avoid numerical difficulties due to bifurcation buckling at the initial state. In the latter period from 1.0 to 2.0, forced displacements are given at the boundary of the surface deformed by initial artificial loads, while applying the downward load equal to self-weight to all members. This deformation process enables us to obtain a curved surface of ABAG [21]. In the following examples, we use pyswarm 0.6 [45], which is a Python library of PSO for optimization, and Abaqus Ver. 2018 [46] for large deformation analysis.

5.1 Examples of Type RH

The initial flat grid of Type RH is composed of 173 reentrant honeycombs with $m = 16$ chevron rods each of which has $n_i = 24$ elements, as illustrated in Fig. 9 (a). The outer connections of the 1st and mth chevron rods are supported by roller that can move in y-direction. Forced displacements 0.30 m are given at all supports on the 1st and mth chevron rods as shown with arrows in 9(a).

The sizes in x-directions of the optimal initial flat grids are 9.0000 m for all cases, and those in y-directions of RHs 1, 2, and 3 are 7.4243 m, 7.7977 m, and 9.0115 m, respectively.

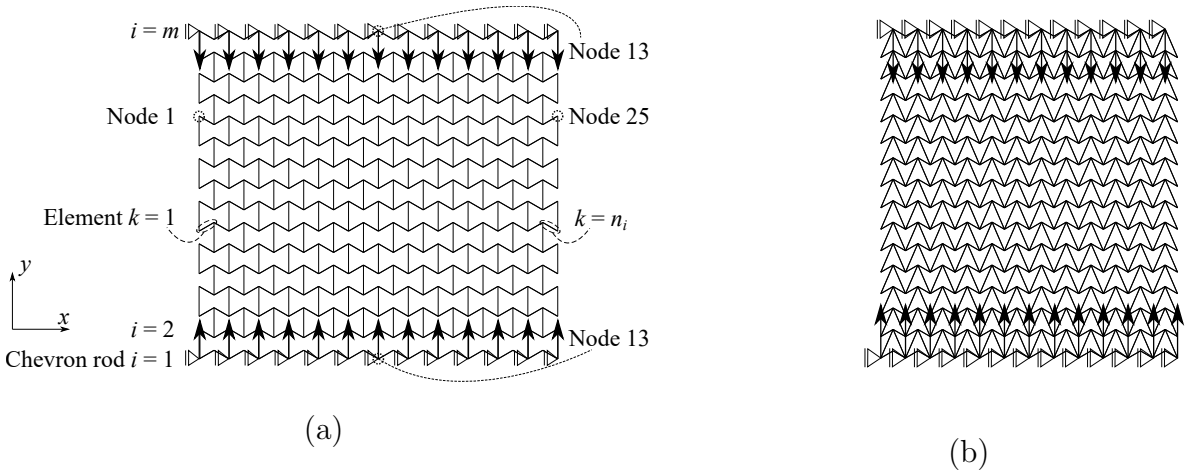

Figure 9: Boundary conditions and forced displacements (arrow); (a) Type RH, (b) Type RT.

The results of RHs 1–3 are shown in Figs. 10–12, respectively. Figure 10(a) and the upper figures in Fig. 12 show the discrete Gaussian curvatures at nodes on the curved surfaces, where the target nodes are indicated by the grey area. As can be seen from these figures, the distributions of discrete Gaussian curvature are almost symmetric with respect to a plane parallel to yz-plane, since the distributions of cross-sectional heights are symmetric. Figures 10(b), (c) and (d) show distributions of cross-sectional heights of elements of chevron rod, and the projection of the curved surfaces onto xz- and yz-planes, respectively. Figure 11 and the lower figures in Fig. 12 show the shapes after forced deformation with the contour of axial stress of each element, and optimal shape of curved surfaces with contour of z-directional displacement of RHs 2 and 3, respectively. Various ABAGs with reentrant honeycombs are obtained by changing distribution of the target nodes. Table 3 shows the optimal angles $(180/2\pi)\boldsymbol{\theta}$ (deg.) of RHs 1–3.

Figures 13(a), (b), and (c) show the values of K_j of RHs 1, 2, and 3, respectively. The numbers of chevron rods, which have target nodes, are 2, 12, and 4 for RHs 1, 2, and 3, respectively. These figures show that all values of K_j of RHs 1–3 are positive. The chevron rods are numbered in increasing order of y-coordinate. The mean, maximum, and minimum values of K_j of RHs 1, 2, and 3 are shown in Table 4. RH 1 has comparatively large discrete Gaussian curvatures at the target nodes distributed widely in x-direction. The histories of objective function values of RHs 1, 2, and 3 are shown in Fig. 14. Approximate solutions are found within about 2/3 of the total iterations. The optimal solutions of RHs 1–3 are obtained

Table 3: Optimal angles $(180/2\pi)\boldsymbol{\theta}$ (deg.) of RHs 1–3 and RTs 1–3.

i	RH 1	RH 2	RH 3	RT 1	RT 2	RT 3
1	40.0000	14.7488	13.7760	12.0472	31.0229	0.0000
2	30.2662	27.4255	24.3656	50.0000	50.0000	34.7531
3	39.9802	21.4771	7.4422	50.0000	50.0000	6.2228
4	40.0000	32.3327	14.2857	46.2684	50.0000	8.1381
5	40.0000	40.0000	10.9126	50.0000	11.3319	13.6342
6	40.0000	40.0000	7.0731	21.1182	14.1451	11.3380
7	40.0000	39.7786	40.0000	34.2966	23.9030	50.0000
8	17.3203	32.3755	0.0000	8.3701	21.9299	25.2091
9	12.6809	39.7769	40.0000	7.9463	49.2106	26.4698
10	39.1963	28.4857	31.7535	16.6086	43.5232	44.6211
11	40.0000	32.5705	40.0000	26.7399	13.1501	32.1896
12	40.0000	38.8833	0.0000	42.6460	17.1515	50.0000
13	35.5555	25.2261	40.0000	50.0000	9.1816	29.9167
14	40.0000	22.7660	0.0000	22.9564	39.1471	16.3895
15	40.0000	38.8350	40.0000	0.0924	50.0000	50.0000
16	10.0372	28.9499	0.0000	50.0000	37.3468	1.1488

Table 4: Mean, maximum, and minimum values of discrete Gaussian curvatures at the target nodes ($\times 10^{-3}$ $(1/\mathrm{m}^2)$).

	RH 1	RH 2	RH 3	RT 1	RT 2	RT 3
Mean	15.4336	6.8785	5.8467	6.1106	2.0966	4.1352
Max.	16.0029	9.6618	7.5583	6.7981	4.6344	5.8518
Min.	15.0946	5.7211	4.9573	5.6182	1.4762	4.1352

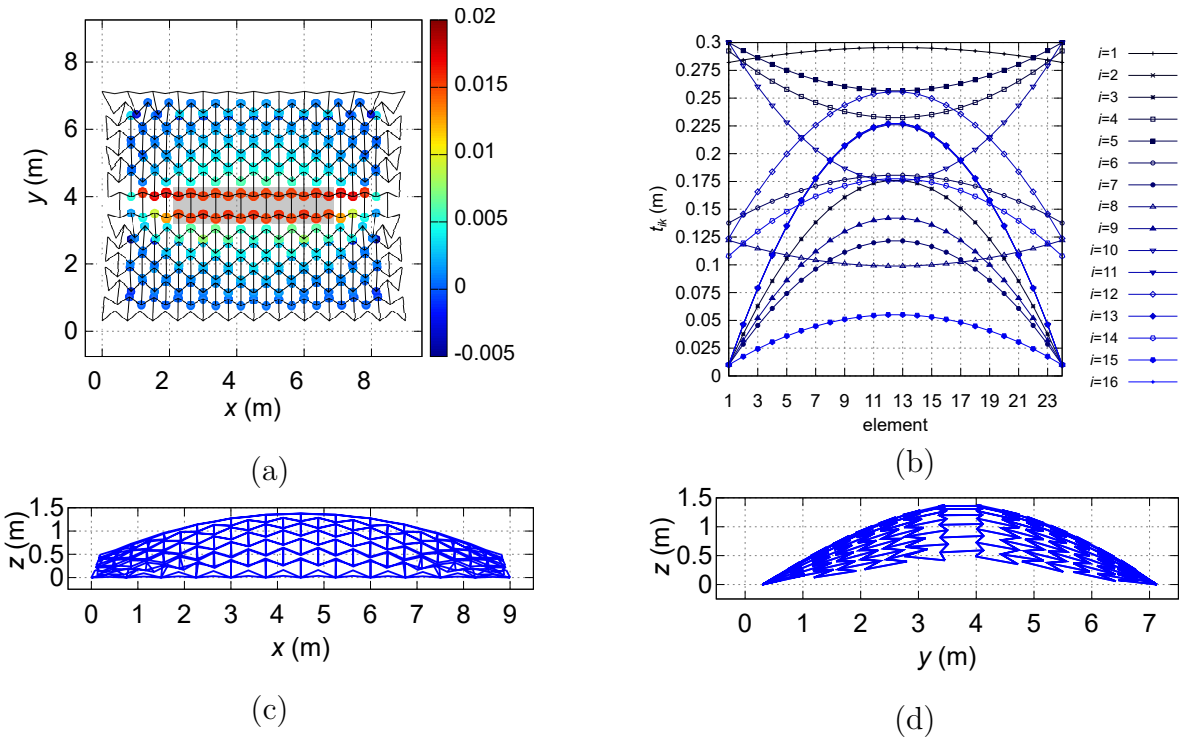

Figure 10: Optimal surface and the distribution of discrete Gaussian curvature of RH 1; (a) discrete Gaussian curvature and target nodes (grey area), (b) cross-sectional heights of chevron rods, (c) surface projected onto xz-plane, (d) surface projected onto yz-plane.

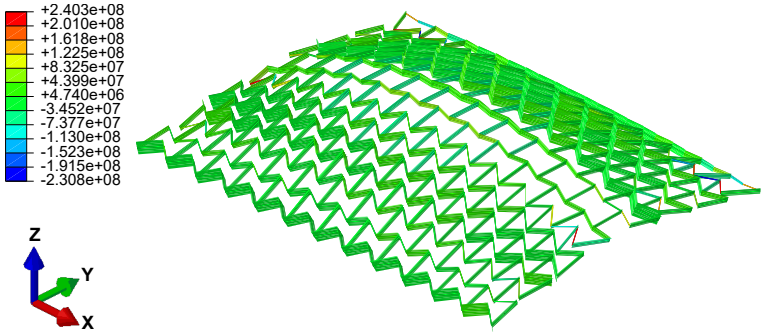

Figure 11: Shape of RH 1 after forced deformation (contour: axial stress (Pa)).

at the iteration 30.

5.2 Examples of Type RT

The initial flat grid of Type RT is composed of 345 reentrant triangles with $m = 16$ chevron rods that have $n_i = 24$ $(i = 1, \ldots, 15)$ and $n_m = 22$ elements, as illustrated in Fig. 9(b). The outer connections of the 1st and mth chevron rods are supported by roller that can move in

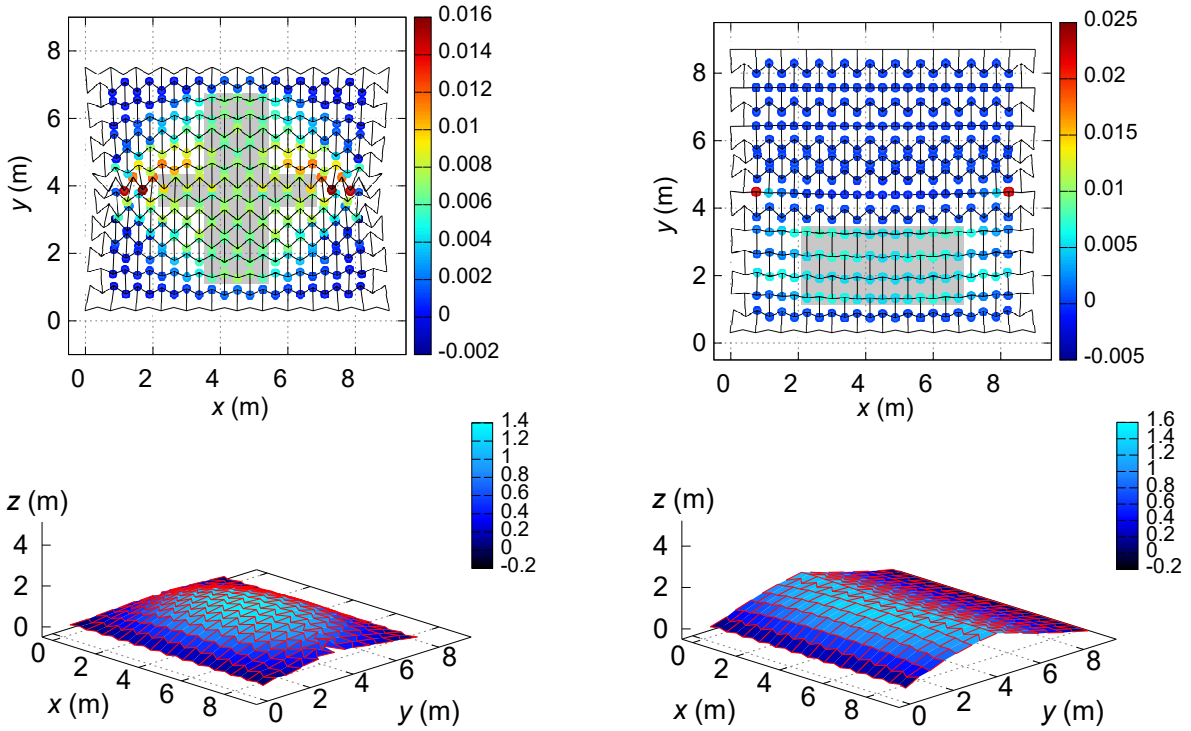

(a) (b)

Figure 12: Comparison of the distribution of discrete Gaussian curvature and optimal shape of RHs 2 and 3. Distribution of discrete Gaussian curvature at internal nodes including the target nodes in grey area in the upper figure. Optimal shape after forced deformation in the lower figure with contour of z-directional displacement. (a) RH 2, (b) RH 3.

y-direction. Forced displacements 0.30 m are given at all supports on the 1st and mth chevron rods. The arrows in Fig. 9(b) represent the directions of the forced displacements.

The sizes in x-directions of the optimal initial flat grids are 7.2000 m for all cases, and those in y-directions of RTs 1, 2, and 3 are8.1518 m, 8.0232 m, and 7.8002 mMicropolar Modeling of Auxetic Chiral Lattices with Tunable Internal Rotation, respectively. The results of RTs 1–3 are shown in Figs. 15–17. Figure 15(a) and the upper figures in Fig. 17 show the discrete Gaussian curvatures at nodes on the curved surfaces, where the target nodes are indicated by the grey area. Figures 15(b), (c) and (d) show distributions of cross-sectional heights of elements of chevron rod, and the projection of the curved surface onto xz- and yz-planes, respectively. As can be seen from these figures, the distributions of discrete Gaussian curvature are almost symmetric with respect to a plane parallel to yz-plane. The distributions of discrete

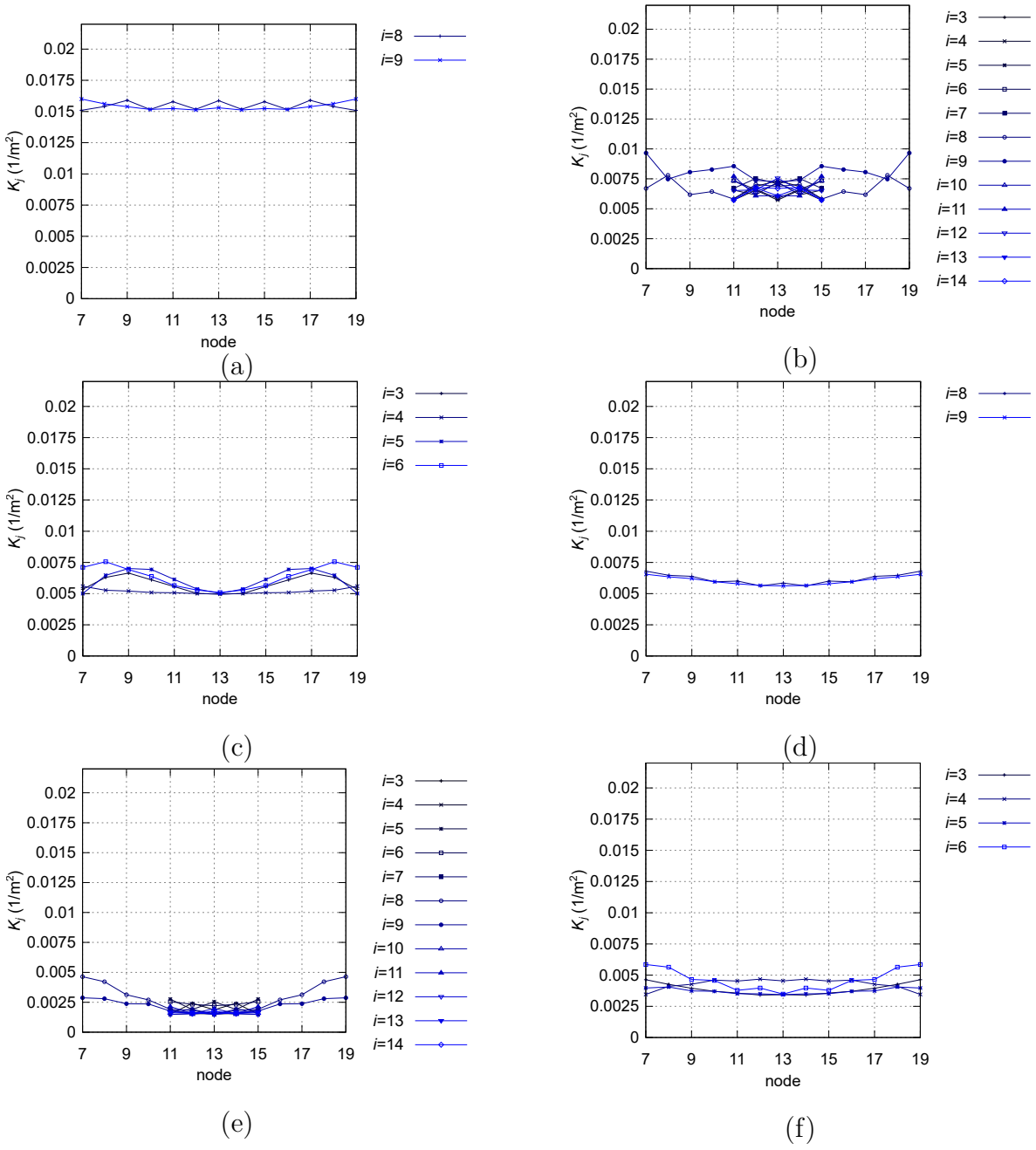

Figure 13: Distribution of discrete Gaussian curvature K_j at target nodes, (a) RH 1 , (b) RH 2, (c) RH 3, (d) RT 1, (e) RT 2, (f) RT 3.

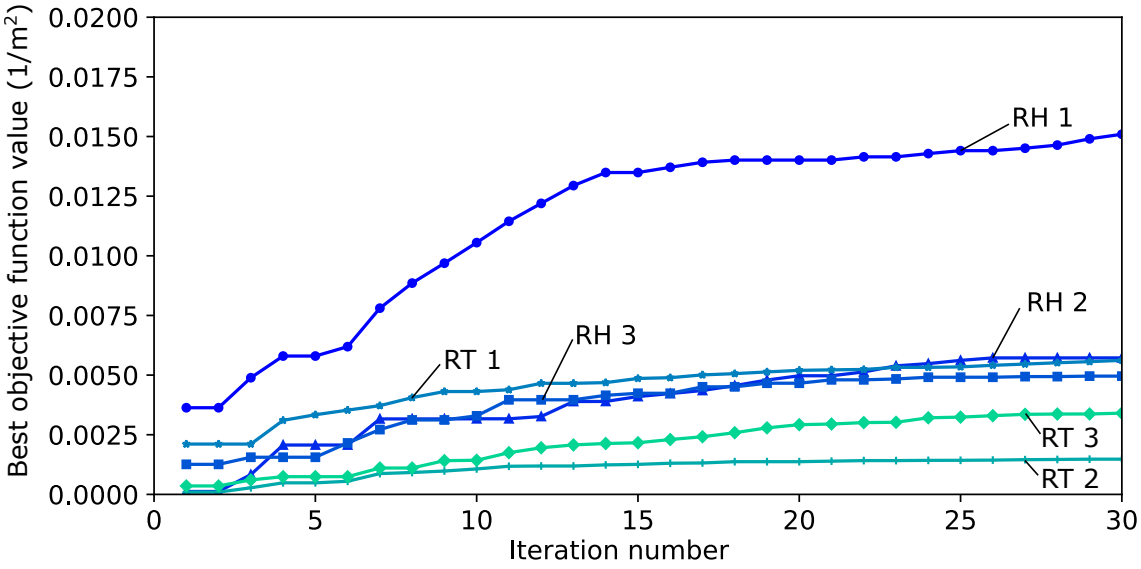

Figure 14: Iteration histories of objective function of RHs 1–3 and RTs 1–3.

Gaussian curvature of RTs 1 and 2, which have symmetric arrangements of target nodes, are obviously antisymmetric with respect to a plane parallel to xz-plane. Various ABAGs with reentrant triangles are obtained by changing distribution of the target nodes. Table 3 shows the optimal angles $(180/2\pi)\boldsymbol{\theta}$ (deg.) of RTs 1, 2, and 3.

Figures 13(d), (e), and (f) show the values of K_j of RTs 1, 2, and 3, respectively. The numbers of the chevron rods, which have target nodes, are 2, 12, and 4 for RTs 1, 2, and 3, respectively. These figures show that all values of K_j of RTs 1–3 are positive. The mean, maximum, and minimum values of K_j of RTs 1, 2, and 3 are shown in Table 4. These results show that the optimal shape of RT 2 has smaller discrete Gaussian curvatures at target nodes than the other examples of Type RT, because the target nodes are distributed widely in y-direction. By contrast, RT 1 has comparatively large discrete Gaussian curvatures at the target nodes distributed widely in x-direction. The histories of objective function values of RTs 1, 2, and 3 are shown in Fig. 14. Approximate solutions are found within about 2/3 of the total iterations. The optimal solutions of RTs 1–3 are obtained at the final iteration 30.

5.3 Validation for optimal solution for RH 1

To validate the result of optimal surface of RH 1 obtained by PSO, the result is compared with those obtained by two other metaheuristic methods, namely, GA and SA. In the following

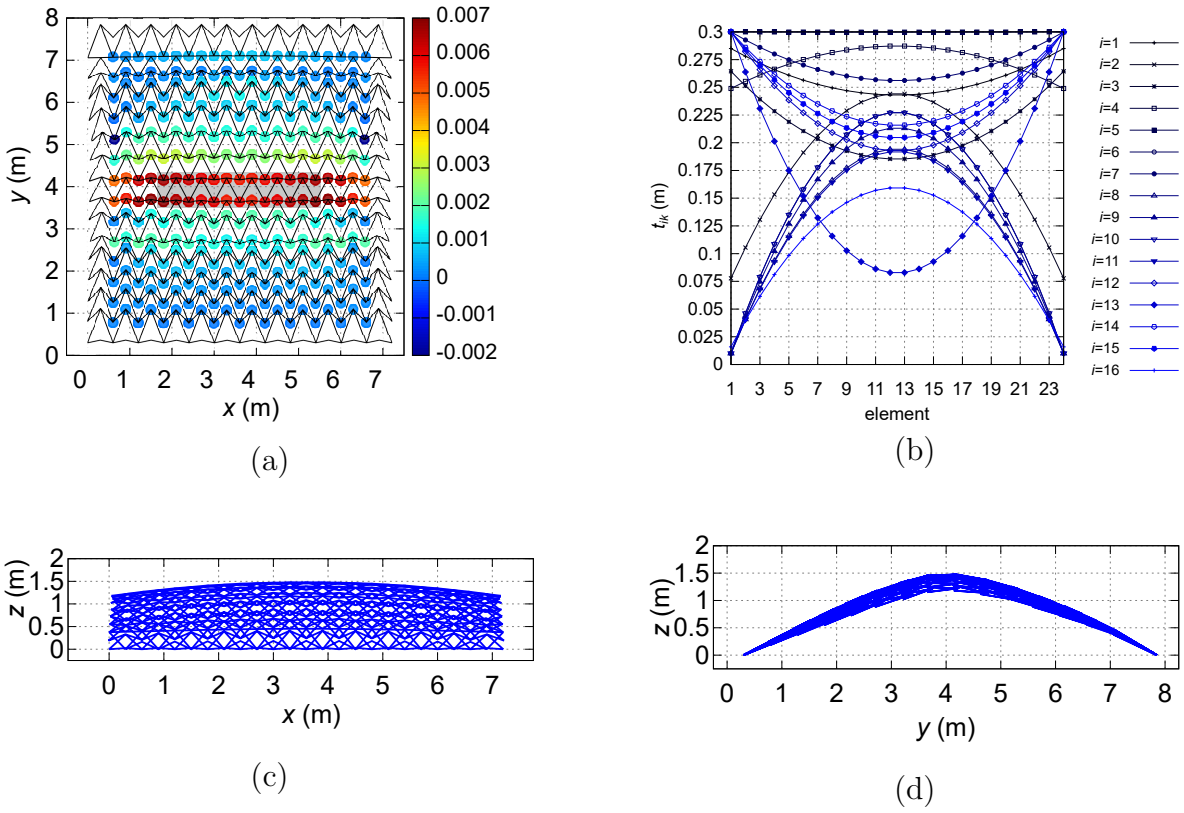

Figure 15: Optimal surface and the distribution of discrete Gaussian curvature of RT 1; (a) discrete Gaussian curvature and target nodes (grey area), (b) cross-sectional heights of chevron rods, (c) surface projected onto xz-plane, (d) surface projected onto yz-plane.

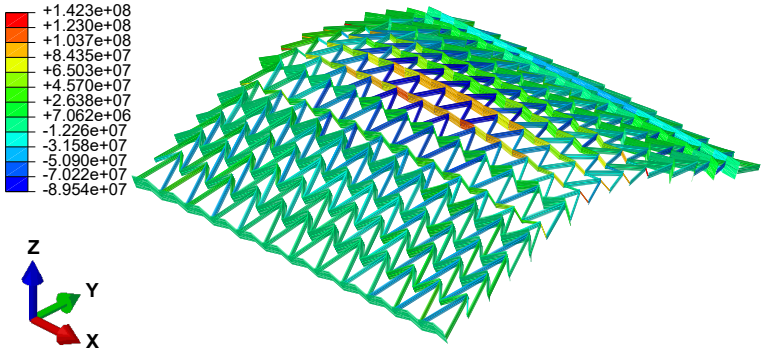

Figure 16: Shape of RT 1 after forced deformation (contour: axial stress (Pa)).

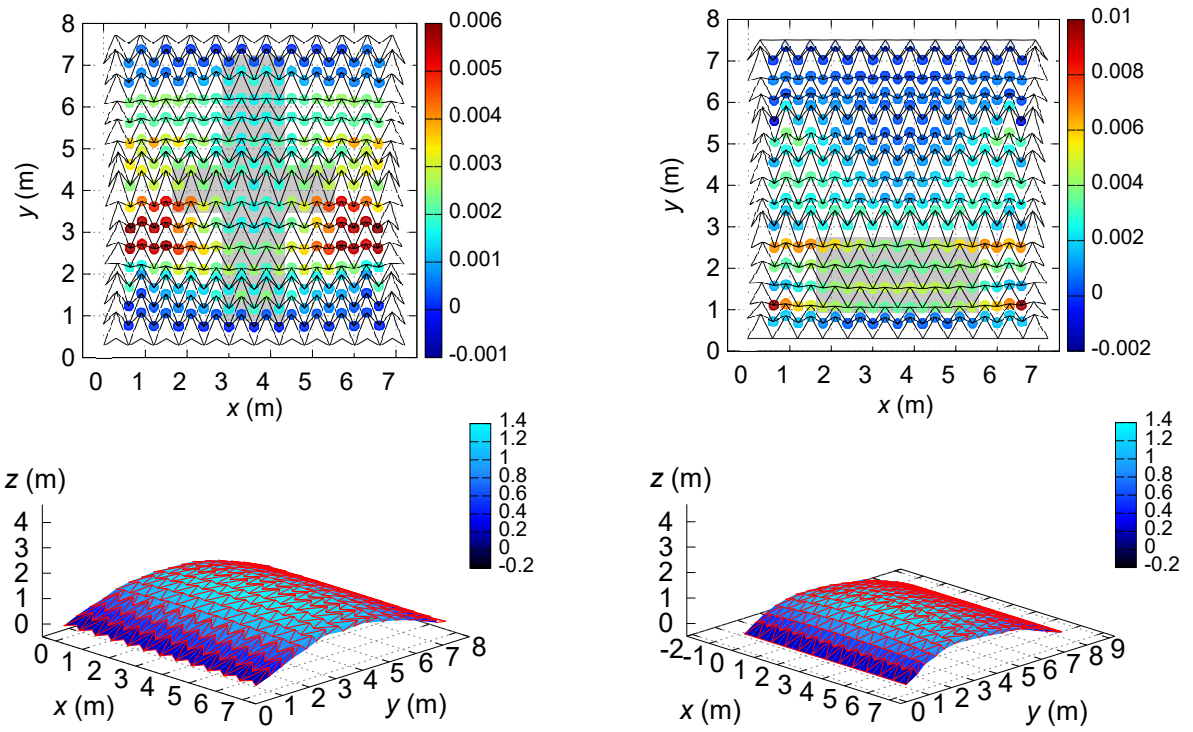

(a) (b)

Figure 17: Comparison of the distribution of discrete Gaussian curvature and optimal shape of RTs 2 and 3. Distribution of discrete Gaussian curvature at internal nodes including the target nodes in grey area in the upper figure. Optimal shape after forced deformation in the lower figure with contour of z-directional displacement. (a) RT 2, (b) RT 3.

examples, we use DEAP [38] and dual annealing [40], which are libraries of GA and SA, respectively, for Python. Parameters of GA and SA are shown in Table 5. Computation is carried out on a PC with Intel Core i7-8700 CPU 3.20 GHz, 16.0GB RAM and six cores.

Table 6 shows the optimal objective function values and computation time of RH 1. When PSO is used, the computation time is the smallest, and the objective function value is close to that of SA, which is the largest among three methods. The objective function obtained by using GA is the smallest, and the computation time is about twice that of PSO. Although SA has the best objective function value, SA is not a practical method because the computation time of 277.0 h is too large. Figure 18 compares the surface shapes and distributions of discrete Gaussian curvature of the optimal surfaces of RH 1 obtained by the three methods.

Shapes of deformed surfaces are close to each other, because the design variables θ_8 and θ_9 are smaller than those for the other chevron rods for all the results by the three methods.

Table 5: Parameters of GA and SA.

Method	Parameters	Values
GA	Population size	300
	Probability of mutation	20%
	Probability of crossover	50%
	Maximum number of generations	50
SA	Maximum number of steps	1000
	Initial temperature	5230
	Temperature at starting re-annealing	0.1046

Table 6: Comparison of objective functions of optimal surfaces of RH 1 and computation time.

	PSO	GA	SA
Objective function	0.0151	0.0113	0.0172
Computation time (h)	9.9	20.6	277.0

Therefore, a favorable solution can be obtained no matter which of the three methods is used for solving the problem.

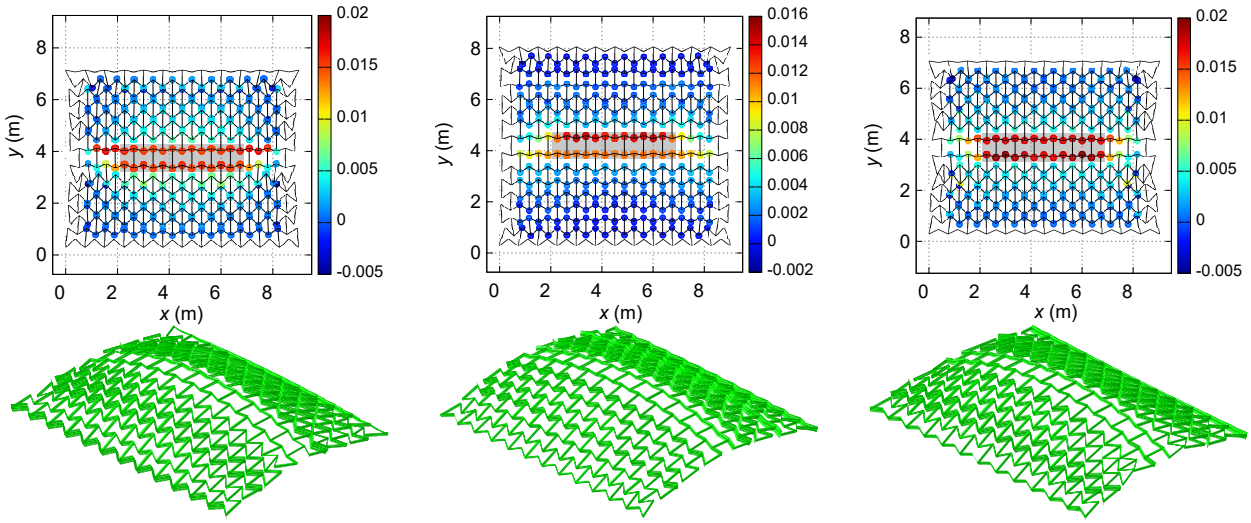

(a) (b) (c)

Figure 18: Distributions of discrete Gaussian curvature and deformed surfaces of RH 1 obtained by the three different metaheuristics; (a) PSO, (b) GA, (c) SA.

6 Conclusions

An optimization method has been proposed for design of ABAG, which is a curved surface generated by assigning forced displacements to the initially planar grid with negative Poisson's ratio for in-plane deformation. Since ABAG is one of the auxetic structures, positive values of Gaussian curvature are mainly distributed on the obtained surfaces through large-deformation analysis. We formulate the optimization problem using discrete Gaussian curvature and discrete mean curvature vector, which are invariants defined in discrete differential geometry.

An ABAG is discretized into triangles for computing discrete curvatures. Triangular mesh is generated using the nodes on the connections between members. An initial flat grid of ABAG is composed of reentrant honeycomb or reentrant triangle composed of two types of members: the chevron rods and the tie rods. A chevron rod that has a zigzag shape generates convexity and concavity on a curved surface utilizing its bending and torsional deformation. On the other hand, a tie rod connects the neighboring chevron rods. Discrete Gaussian curvature, which is defined by the angle defect from a flat shape, can evaluate the norm of convexity and concavity from surrounding nodes on ABAG. Discrete mean curvature vector, which is formulated by cotangent formula, is used as constraints for direction of convexity at each node.

The optimization problem has been formulated for obtaining the surface with specified convex region where partly maximized value of discrete Gaussian curvature. The objective function is the minimum value of discrete Gaussian curvatures of the target nodes. The design variables are the angles between x-axis and the left ends of the chevron rods, and the Bernstein coefficients designing distributions of the cross-sectional heights of chevron rods. To reduce the number of design variables while keeping the smoothness of the solution, we formulate the distribution of cross-sectional heights by cubic Bernstein polynomials. The optimization problem is solved using the PSO which is a population-based derivative-free method. Dependence of the results on the parameter values of the PSO has been investigated, and it has been shown by comparing the results with those by GA and SA that a good approximate optimal solution can be found with a reasonable computational cost using PSO.

Optimization results have been shown for the six numerical examples, which are designed by reentrant honeycomb or reentrant triangle. By using the proposed method, the designer can obtain surfaces with different shapes under the same boundary conditions and forced dis-

placements by changing the assignment of the target nodes on an ABAG. The results show that the norm of discrete Gaussian curvature depends on the loading conditions and distributions of the target nodes. Although the optimal cross-sectional heights and angle $\boldsymbol{\theta}$ of chevron rods have complex distributions depending on the loading conditions and the assignments of the target nodes, this fact verifies that the proposed optimization method is useful to obtain unexpected optimal solutions of ABAGs, which have the different mechanical properties from those expected by our intuition. The proposed method using discrete differential geometry can be effectively applied to design of ABAG for dome-like architectural roof.

Acknowledgment

This research is partly supported by JSPS KAKENHI Number JP19J20405 and JST CREST Grant Number JPMJCR1911.

Appendix: Particle Swarm Optimization

Particle Swarm Optimization (PSO) is a metaheuristic method that mimics foraging behavior patterns by a group of organisms such as birds and fish, and was proposed by Kennedy and Eberhart [39]. In the PSO method, a large number of solutions $\boldsymbol{x}$, called particles, search the optimal solution globally in a multidimensional space. Since the update of the solutions does not depend on the gradient of the objective function $F(\boldsymbol{x})$, the method is effective for problems where the objective function $F(\boldsymbol{x})$ is not differentiable. Each particle has its position and velocity, and particles exchange information with each other and determine the search directions based on the velocities defined as the sum of the vectors of position and velocity. The algorithm of PSO is shown below.

Algorithm of PSO:

Step 1: Initialize randomly the positions $\boldsymbol{x}_J^0 = \{x_{J_1}^0, \ldots, x_{J_D}^0\}$ and vectors $\boldsymbol{v}_J^0 = \{v_{J_1}^0, \ldots, v_{J_D}^0\}$ $(J = 1, \ldots, M; D = 1, \ldots, 3m)$ based on the upper and lower bounds of design variables. Here, $3m$ is the total number of design variables representing $\boldsymbol{\theta}$, $\boldsymbol{\beta}_0$, and $\boldsymbol{\beta}_1$, as shown in Sec. 4.2, and M is the number of solutions (particles).

Step 2: Let $\boldsymbol{x}_{\mathrm{p},J}^{\gamma}$ and $\boldsymbol{x}_{\mathrm{g}}^{\gamma}$ denote the personal best position of the Jth particle and the global best position of all particles, respectively, at iteration γ. Initialize as $\gamma = 0$ and $\boldsymbol{x}_{\mathrm{p},J}^{0} = \boldsymbol{x}_{J}^{0}$ for $J = 1, \ldots, M$. Set $\boldsymbol{x}_{\mathrm{g}}^{0}$ as the particle that has the maximum objective function value among all particles, and $J = 1$.

Step 3: Velocities and positions of the Jth particle at iteration γ are updated as:

$$\begin{aligned} \boldsymbol{v}_{J}^{\gamma+1} &= \omega \boldsymbol{v}_{J}^{\gamma} + c_1 r_1 \left(\boldsymbol{x}_{\mathrm{g}}^{\gamma} - \boldsymbol{x}_{J}^{\gamma} \right) + c_2 r_2 \left(\boldsymbol{x}_{\mathrm{p},J}^{\gamma} - \boldsymbol{x}_{J}^{\gamma} \right) \\ \boldsymbol{x}_{J}^{\gamma+1} &= \boldsymbol{x}_{J}^{\gamma} + \boldsymbol{v}_{J}^{\gamma+1} \end{aligned}$$

The inertia weight ω tunes the contribution of velocity $\boldsymbol{v}_{J}^{\gamma}$. We use the parameters c_1 and c_2 as the ratios of the particles which do not move toward the global and personal best ones, and r_1 and r_2 as random numbers in the range of $0 \leq r_1 \leq 1$ and $0 \leq r_2 \leq 1$, respectively.

Step 4: Compute the objective function $F(\boldsymbol{x}_{J}^{\gamma+1})$.

Step 5: If $F(\boldsymbol{x}_{J}^{\gamma+1}) > F(\boldsymbol{x}_{\mathrm{p},J}^{\gamma})$, update as $\boldsymbol{x}_{\mathrm{p},J}^{\gamma} \leftarrow \boldsymbol{x}_{J}^{\gamma+1}$ and go to Step 6; otherwise, update $J \leftarrow J + 1$ and go to Step 3.

Step 6: If $F(\boldsymbol{x}_{\mathrm{p},J}^{\gamma+1}) > F(\boldsymbol{x}_{\mathrm{g}}^{\gamma})$, update $\boldsymbol{x}_{\mathrm{g}}^{\gamma} \leftarrow \boldsymbol{x}_{\mathrm{p},J}^{\gamma+1}$. If $J < M$, update $J \leftarrow J + 1$ and go to Step 3. If the convergence criterion is satisfied or γ is equal to the iteration limit, go to Step 7; otherwise, set $J = 1$ and go to Step 3.

Step 7: Terminate the algorithm and output $\boldsymbol{x}_{\mathrm{g}}^{\gamma+1}$ as the optimal solution.

Table 7 shows 36 sets of parameters of PSO and the corresponding objective functions of RH 1. The inertia weight ω can be set as a value larger than 1.00; however, infeasible solutions are obtained when $\omega \geq 1.25$. Therefore, we compared the objective function values obtained by using parameters $\omega \in \{0.25, 0.50, 0.75, 1.00\}, c_i \in \{0.25, 0.50, 0.75\}$ $(i = 1, 2)$, and found that the set of parameters $\omega = 0.75, c_1 = 0.75, c_2 = 0.50$ leads to the largest objective function value.

Table 7: Parameters of PSO and objective functions of RH 1.

ω	c_1	c_2	objective function F	ω	c_1	c_2	objective function F
		0.25	0.0073			0.25	0.0117
	0.25	0.50	0.0066		0.25	0.50	0.0130
		0.75	0.0063			0.75	0.0114
		0.25	0.0093			0.25	0.0139
0.25	0.50	0.50	0.0077	0.75	0.50	0.50	0.0146
		0.75	0.0068			0.75	0.0137
		0.25	0.0083			0.25	0.0151
	0.75	0.50	0.0089		0.75	0.50	0.0151
		0.75	infeasible			0.75	0.0139
		0.25	0.0082			0.25	0.0114
	0.25	0.50	0.0086		0.25	0.50	0.0099
		0.75	0.0080			0.75	0.0109
		0.25	0.0093			0.25	0.0141
0.50	0.50	0.50	0.0102	1.00	0.50	0.50	0.0125
		0.75	0.0106			0.75	0.0109
		0.25	0.0137			0.25	0.0114
	0.75	0.50	0.0124		0.75	0.50	0.0123
		0.75	0.0130			0.75	0.0132

References

[1] Evans KE. Auxetic polymers: A new range of materials. Endeavour 1991;15(4):170-174.

[2] Lakes R. Foam structures with a negative Poisson's ratio. Science 1987;235(4792):1038-1040.

[3] Liu Y, Hu H. A review on auxetic structures and polymeric materials. Scientific Research and Essays 2010;5(10):1052-1063.

[4] Ju J, Summers JD. Compliant hexagonal periodic lattice structures having both high shear strength and high shear strain. Material Design 2011;32(2):512-524.

[5] Grima JN, Caruana-Gauci R, Attard D, Gatt R. Three-dimensional cellular structures with negative Poisson's ratio and negative compressibility properties. Physical and Engineering Science 2012;468:3121-3138.

[6] Gibson LJ, Ashby MF. Cellular solids: structure and properties. Cambridge: Cambridge University Press; 1999.

[7] Hou Y, Tai YH, Lira C, Scarpa F, Yates JR, Gu B. The bending and failure of sandwich structures with auxetic gradient cellular cores. Composites: Part A 2013;49:119-131.

[8] Evans KE, Alderson A. Auxetic materials: Functional materials and structures from lateral thinking!. Adv Mater 2000;12(9):617-628.

[9] Anurag C, Anvesh CK, Harsha AS. Auxetic materials. International Journal for Trends in Engineering & Technology 2015;5(2):156-160.

[10] Saxena KK, Das R, Calius EP. Three decades of auxetics research - Materials with negative Poisson's ratio: A review. Adv Eng Mater 2016;18(11):1847-1870.

[11] Larsen UD, Sigmund O, Bouwstra S. Design and fabrication of compliant micromechanisms and structures with negative Poisson's ratio. Journal of Micro electromechanical Systems 1997;6(2):99-106.

[12] Bendsøe MP, Sigmund O. Topology optimization 2nd edn. Berlin: Springer; 2003.

[13] Schwerdtfeger J, Wein F, Leugering G, Singer RF, Koner CK. Design of auxetic structures via mathematical optimization. Adv Mater 2011;23:2650-2654.

[14] Kureta R, Kanno Y. A mixed integer programming approach to designing periodic frame structures with negative Poisson' s ratio. Material Design 2014;15(3):773-800.

[15] Ou J, Ma Zhao, Peters J, Dai S, Vlavianos N, Ishii H. KinetiX - designing auxetic-inspired deformable material structures. Computers & Graphics 2018;75:72-81.

[16] Konaković M, Crane K, Deng B, Bouaziz S, Piker D, Pauly M. Beyond developable: Computational design and fabrication with auxetic materials. SIGGRAPH'16 Technical Paper; 2016.

[17] Konaković-Luković M, Panetta J, Crane K, Pauly M. Rapid deployment of curved surfaces via programmable auxetics. ACM Trans Graph 2018;37(4);1-13.

[18] Chen T, Panetta J, Schnaubelt M, Pauly M. Bistable auxetic surface structures. ACM Trans Graph 2021;40(4):1-9.

[19] Rombouts J, Lombaert G, De Laet L, Schevenels M. A novel shape optimization approach for strained gridshells: Design and construction of a simply supported gridshell. Eng Struct 2019;192(1):166-180.

[20] D'amico B, Kermani A, Zhang H. Form finding and structural analysis of actively bent timber grid shells. Eng Struct 2014;81:195-207.

[21] Sakai Y, Ohsaki M. Discrete elastica for shape design of gridshells. Eng Struct 2018;169(15):55-67.

[22] Adriaenssens S, Block P, Veenendaal D, Williams C, (Eds.). Shell Structures for Architecture. London: Routledge; 2004.

[23] Naboni R, Mirante L. Computational design and simulation of bending-active auxetic structures. Gestão e Tecnologia de Projectos 2016;11(2):59-71.

[24] Naboni R, Pezzi SS. Embedding auxetic propoerties in designing active-bending gridshells. SiGraDi; 2016, pp. 720-726.

[25] Naboni R, Sartori S, Mirante L. Adaptive-curvature structures with auxetic materials. Advanced Materials Research 2018;1149:53-63.

[26] Howell LL. Compliant Mechanisms. New York: Wiley; 2001.

[27] La Magna R, Knippers J. Tailoring the bending behaviour of material patterns for the induction of double curvature. Humanizing Digital Reality; 2018, pp. 441-452.

[28] Harris R, Romer J, Kelly O. Design and construction of the Downland Gridshell. Build Res Inf 2003;31:427-454.

[29] Sakai Y, Ohsaki M. Parametric study of non-periodic and hybrid auxetic bending-active gridshells. J of IASS 2020;61(4):275-284.

[30] Fujita S, Ohsaki M. Shape optimization of free-form shells using invariants of parametric surface. Int J Space Struct 2010;25(3):143-157.

[31] Meyer M, Desbrun M, Schöder P, Barr AH. Discrete differential-geometry operators for triangulated 2-manifolds. In: Hege HC, Polthier K, (eds). Visualization and Mathematics III. Berlin: Springer 2003; pp. 35-57.

[32] Pinkall U, Polthier K. Computing discrete minimal surfaces and their conjugates. Experimental Mathematics 1993;2(1):15-36.

[33] Sullivan JM. Curvature measures for discrete surfaces. ACM SIGGRAPH 2005 Courses; 2005.

[34] Nealen A, Igarashi T, Sorkine O, Alexa M. Laplacian mesh optimization. Proc 4th Int Conf on Computer Graphics and Interactive Techniques in Australasia and Southeast Asia (GRAPHITE 06); 2006, pp. 381-389.

[35] Hasançebi O, Çarbas S, Doğan E, Erdal F, Saka MP. Comparison of nondeterministic search techniques in the optimum design of real size steel frames. Comput Struct 2010;88(17-18):1033–48.

[36] Saka MP, HasanÇebi O, Geem ZW. Metaheuristics in structural optimization and discussions on harmony search algorithm. Swarm Evol Comput 2016;28:88–97.

[37] Kaveh A, Javadi SM. Chaos-based firefly algorithms for optimization of cyclically large-size braced steel domes with multiple frequency constraints. Comput Struct 2019;214:28-39.

[38] Fortin FA, De Rainville FM, Parizeau M, Gagné C. DEAP: Evolutionary algorithm made easy, Journal of Machine Learning Research 2012;13:2171-2175.

[39] Kennedy J, Eberhart R. Particle swarm optimization, Proc ICNN'95 – Int Conf on Neural Networks (ICNN95) 1995;4:1942-1948.

[40] `https://docs.scipy.org/doc/scipy/reference/generated/scipy.optimize.dual_annealing.html`

[41] Gibson LJ, Ashby MF, Schajer GS, Robertson CI. The mechanics of two-dimensional cellular materials. Proc R Soc London A: Math Phys Eng Sci 1982;382(1782):25-42.

[42] Masters IG, Evans KE. Models for the elastic deformation of honeycombs. Compos Struct 1996;35(4):403-422.

[43] Lakes RS. Design considerations for materials with negative Poisson's ratios. Journals of Mechanical Design ASME 1993;115:696-700.

[44] Evans KE. The design of doubly curved sandwich panels with honeycomb cores Composite Structures 1993;17(2):95-111.

[45] pyswarm 0.6. Web Site. `https://pythonhosted.org/pyswarm/`

[46] Dassault Systémes. Abaqus User's Manual Ver 2016; 2016.